Labyrinthine acoustic metamaterials with space-coiling channels for low-frequency sound control

Labyrinthine acoustic metamaterials with space-coiling channels for low-frequency sound control

A.O. Krushynska[1,*], F. Bosia[1], N.M. Pugno[2,†]

[1]Department of Physics and Nanostructured Interfaces and Surfaces, University of Torino, Via Pietro Giuria 1, 10125 Torino, Italy

[2]Laboratory of Bio-Inspired and Graphene Nanomechanics, Department of Civil, Environmental and Mechanical Engineering, University of Trento, Via Mesiano 77, 38123 Trento, Italy

14 December 2017

*akrushynska@gmail.com

†nicola.pugno@unitn.it Also at:

(i) School of Engineering and Materials Science, Queen Mary University of London, Mile End Road, London E1 4NS, United Kingdom;

(ii) Ket Labs, Edoardo Amaldi Foundation, Italian Space Agency, Via del Politecnico snc, 00133 Rome, Italy

Abstract

We analyze the potential of fractal space-filling curves for the design of labyrinthine acoustic metamaterials acting as perfect reflectors of low-frequency airborne sound.

Keywords: low-frequency waves, labyrinthine acoustic metamaterial, space-coiling curve, Fabry-Perot resonance, fractal organization, perfect reflector, tortuous porous material.

1. Introduction

Acoustic metamaterials are composites with an engineered structure governing remarkable functionalities, e.g. acoustic cloaking, transformation acoustics, and subwavelength-resolution imagining [1, 2]. Apart from unusual effective properties, the metamaterials offer various possibilities to control propagation of sound or elastic waves at deep sub-wavelength scales [3, 4, 5]. This can be achieved by incorporating heavy resonators [3], Helmholtz resonators [6, 7], tensioned membranes [8, 9], or sub-wavelength perforations or slits [10, 11, 12, 13] into a material structure. A class of acoustic metamaterials with internal slits is also known as "labyrinthine". They have recently attracted considerable attention due to an exceptionally high refractive index and the ability to efficiently reflect sound waves, while preserving light weight and compact dimensions [13, 12, 14].

Labyrinthine metamaterials enable to slow down an effective speed of acoustic waves due to path elongation by means of folded narrow channels [15, 13]. Their high efficiency in manipulating low-frequency sound has been experimentally demonstrated for various channel geometries. For example, Xie et al. [16] have shown the negative effective refractive index at broadband frequencies for labyrinthine metastructures with zig-zag-type channels. For the same configuration, Liang et al [15] have demonstrated extraordinary dispersion, including negative refraction and conical dispersion for low-frequency airborne sound. Frenzel et al. have used the zig-zag channels to achieve broadband sound attenuation by means of three-dimensional labyrinthine metastructures [17, 18]. The issue of poor impedance matching for labyrinthine metamaterials has been addressed by exploiting tapered and spiral channels [19] and hierarchically structured walls [20].

Cheng et al. have proven almost perfect reflection of low-frequency sound by sparsely arranged unit cells with circular-shaped channels that can induce artificial subwavelength Mie resonances [12]. In our previous work, we have proposed a simple modification to the later design (by adding a square frame) to achieve a tunable functionality [14]. Moleron et al. have emphasized the importance of thermo-viscous effects on the performance of labyrinthine structures with sub-wavelength slits [21].

Most of the mentioned studies analyze metamaterials with curved channels, in which the direction of wave propagation coincides with that for incident waves. In this case, a folded channel behaves as a straight slit of effective length L_{eff}, which approximately equals to the shortest path taken by the wave to pass through the structure [13, 21]. Thus, a channel tortuosity appears to play no role. Possible effects of the path tortuosity, when a wave is allowed to propagate in an opposite direction relative to that of the incident field, remain not investigated yet. A few papers have analyzed labyrinthine metamaterials of such a type of channels. In [19], Xie metamaterials with spiral channels have been investigated to enable tunability of effective structural parameters, such as refractive index and impedance. Hierarchically organized channel walls have shown to achieve a broadband wave absorption [20]. These works are focused on experimental validation of the mentioned features, and lack a theoretical analysis of wave behavior in a tortuous channel.

The goal of this work is to investigate numerically dispersion and propagation properties of low-frequency airborne sound in labyrinthine metamaterials with channels, which allow changing the direction of wave propagation. To this purpose, we design sub-wavelength paths in metamaterial unit cells along a fractal curve of various iteration levels. In

particular, we consider a space-filling curve for the channel design due to its self-similar organization, clear algorithm for the length elongation, and the ability to fill in an occupied area. We provide a complete theoretical analysis of the wave dispersion in the designed metamaterials complemented by the study of acoustic transmission, reflection, and absorption for a monoslab in the absence or presence of thermos-viscous losses. Our results demonstrate that, when a wave inside a narrow channel is allowed to propagate in the opposite (relative to the incident wave front) direction, the wave dynamics is not equivalent to that in a straight slit of an effective length. The peculiar channel tortuosity allows opening wide sub-wavelength band gaps. At band gap frequencies, total broadband wave reflection occurs that is not influenced by the presence of losses in air. Therefore, the proposed labyrinthine metamaterials have a great potential as efficient reflectors for low-frequency airborne sound. Moreover, to facilitate practical exploitation of these metamaterials, we propose to assemble reconfigurable structures from equi-thickness thin panels (sheets) that is a cheap alternative to an additive manufacturing technique.

2. Space-filling curves

As mentioned above, the wave path is elongated by exploiting the fractal structure of space-filling curves [22]. First space-filling curves were discovered by Peano [23] (later named after him), and since then many other curves were proposed [24]. An attractive property of these curves is that they go through every point of a bounding domain for an unlimited number of iterations. After initially being studied as a curiosity, nowadays space-filling curves are widely applied, e.g. for indexing of multi-dimensional data [25], transactions and disk scheduling in advanced databases [26], building routing systems [27], etc.

Among various space-filling curves, we have chosen the Wunderlich two-dimensional curve filling a square [22], which is constructed as follows. At the 1st iteration level, one draws an "S"-shaped curve starting at the bottom-left corner of a bounding square and ending at the top-right corner. At the n^{th} ($n \geq 2$) iteration level, 3 copies of the $(n-1)^{th}$-level curve are arranged along each side of a square with every copy being rotated by 90° relative to the previous one. The curves are joined into an N-shaped route starting from the up-direction for the left column, then down for the middle column, and finally again up for the right column. At every iteration level N, the length of the Wunderlich curve is $(3^N - 1/3^N)$, while that of e.g. Hilbert's curves is $(2^N - 1/2^N)$ [22]. Faster length elongation enables more compact channel folding in a labyrinthine structure (and thus, increases the tortuosity effect, as will be shown later) that justifies the choice of the Wunderlich curve for this study.

3. Models and analysis methods

Figure 1 presents square labyrinthine unit cells with an internal channel shaped along the Wunderlich curve of one of the three iteration levels, i.e "unit cell 1" (UC1), "unit cell 2" (UC2), and "unit cell 3" (UC3). The structural material is aluminum with mass density $\rho_{Al} = 2700$ kg/m^3 and speed of sound $c_{Al} = 5042$ m/s. The thickness of bounding walls is fixed for all the unit cells and equals d=0.5mm.

The channel width is w, and the size of a square domain occupied by a single labyrinth is $a = 3^N \cdot (w + d) + d$, where N is the iteration level. We preserve an interconnecting cavity of width w between adjacent labyrinths. Thus, the metamaterials unit cell size is $a_{uc} = a + w$ (see Fig. 1a).

We analyze plane waves propagating in the plane of a unit cell cross-section. The metamaterial geometry is assumed to be

constant in the out-of-plane direction without a possibility to excite a momentum in this direction. Hence, the pressure field is always constant in the out-of-plane direction, and the wave dynamics can be analyzed by considering a two-dimensional (2D) geometry. The validity of this assumption is proven by a good agreement with the results of three-dimensional (3D) simulations given in the "Results and Discussion" section.

First, we analyze sound wave dispersion in the labyrinthine metamaterials that are infinite in both in-plane directions. By neglecting any losses in air, small-amplitude variations of harmonic pressure $p(\boldsymbol{x},t)=p(\boldsymbol{x})e^{i\omega t}$ (with angular frequency $\omega=2\pi f$, where f the frequency in Hz) are governed by the homogeneous Helmholtz equation:

$$\nabla\cdot\left(-\frac{1}{\rho_0}\nabla p\right)-\frac{\omega^2 p}{\rho_0 c_0^2}=0 \qquad (1)$$

with air density $\rho_0=1.225$ kg/m^3 and speed of sound $c_0=343$ m/s at temperature $T=20$℃. Since characteristic acoustic impedance of aluminum is around 3e4 times larger than that of air, we assume the structural walls being motionless and apply sound-hard boundary conditions at air-structure interfaces. The pressure distribution at opposite unit cell boundaries is constraint by the Floquet-Bloch periodic conditions:

$$p(\boldsymbol{x}+\boldsymbol{a})=p(\boldsymbol{x})e^{i\boldsymbol{k}\cdot\boldsymbol{a}} \qquad (2)$$

with $\boldsymbol{a}=(a_{uc},a_{uc},0)$ and wave vector $\boldsymbol{k}=(k_x,k_y,0)$. More details about the dispersion analysis can be found in [14].

Next, we evaluate homogeneous wave propagation through a metamaterial monolayer. The analyzed model is given in Fig. 2. Plane wave radiation occurs at the left domain boundary at distance $10a_{uc}$ from the slab. At the right boundary, a perfectly matched layer of width $2a_{uc}$ is attached to eliminate unnecessary wave reflection. At the bottom and top boundaries, the Floquet-Bloch periodic boundary conditions (2)

enable to artificially extend the air domain in the vertical direction. The reflection $R = |p_r/p_i|^2$, transmission $T = |p_t/p_i|^2$, and absorption $A = 1 - R - T$ coefficients are evaluated by averaging incident p_i, reflected p_r, and transmitted p_t pressure fields along the lines located at distance a_{uc} from the metastructure.

In order to analyze how the length and tortuosity of a labyrinthine channel influences sound wave characteristics, we compare T and A values for the metastructures with those for straight slits of width w in solid blocks of length $L=L_{eff}$ or $L=a$, which are distributed at distances a along the vertical direction. In the case of $L=a$, the blocks act as solid scatterers of the same size as labyrinthine structures, but without internal channels. The effective channel length L_{eff} is approximately equal to the shortest wave path from the input to the output through a labyrinthine channel (as shown e.g. by green line in Fig. 1a).

If a channel width is small compared to the wavelength of a propagating wave, thermal and viscous boundary layers near solid walls cause loss effects (*lossy* air). The thickness of these layers decreases with increase of frequency. The thickness of thermal boundary layer δ_{th} is evaluated as follows:

$$\delta_{th} = \sqrt{\frac{k}{\pi f \rho_0 C_p}}, \quad (3)$$

where $k = 25.8$ mW/(m·K) is thermal conductivity, and $C_p = 1.005$ kJ/(m^3·K) is heat capacity at constant pressure. The thickness of viscous boundary layer δ_{vis} is

$$\delta_{vis} = \sqrt{\frac{\mu}{\pi f \rho_0}}, \quad (4)$$

with dynamic viscosity $\mu = 1.814$e-5 Pa·s. The graphical representation of the relations (3), (4) is given in Fig. 3. At 20°C and 1 atm, the viscous and thermal boundary layers' thicknesses are 0.22mm and 0.26mm at 100 Hz, respectively.

As the designed labyrinthine channel are relatively easy to model, we directly

include thermal conduction and viscous attenuation into the governing equations. Thus, the linearized system composed of Navier-Stokes equation, a continuity equation, and an energy equation is solved for acoustic pressure variations p, the fluid velocity variations $\boldsymbol{u}$, and the acoustic temperature variations T. The mentioned variations describe small harmonic oscillations around a steady state. The corresponding equations are given in [28] and implemented in Thermoacoustic interface of Comsol Multiphysics [29].

The dispersion and transmission analyses are performed by means of the finite-element method as eigenvalue and frequency domain simulations in Comsol Multiphysics [29]. Acoustic domains are discretized with the maximum element size of $\lambda_{min}/12$, where $\lambda_{min} = c_0/f_{max}$, and f_{max} is the maximum analyzed frequency. This mesh resolves the smallest wavelength of the study with 12 elements. To properly capture the wave field variations within the viscous and thermal boundary layers, we implemented a frequency-varying mesh with 3-5 boundary layers along the thickness of a viscous layer.

4. Results and discussion

We consider the described labyrinthine metamaterials of two dimensions. In the first case, defined as a "fixed channel" case, we imply a constant channel width, $w = const$, at each iteration step. Thereby we aim at evaluating effects of the path tortuosity on sound propagation with the increase of the path length. For w=4 mm, the metamaterial unit cell sizes a_{uc} are 18 mm for UC1, 45 mm for UC2, and 126 mm for UC3. For another case, called "fixed unit cell" case, we assume a fixed unit cell size, $a_{uc} = const$, with the channel width becoming smaller at each iteration. In particular, we fix $a_{uc} = 14$ mm that corresponds to the channel width $w = 3$ mm for UC1 and 0.9mm for UC2. For UC3, the internal channel is

eliminated for the wall thickness d=0.5 mm. For the specified value of a_{uc}, the channel width in the "fixed unit cell" case is smaller than that in the "fixed channel" case for the same iteration level. Thus, by comparing wave propagation for these two cases, we can evaluate how different amount of thermo-viscous losses influences wave propagation in similar structured labyrinthine channels.

In the both cases, an internal unit cell channel is shaped along the Wunderlich curve. However, the channel length is different from the length of the Wunderlich curve due to deviations in the construction approaches. In particular, the algorithm of the Wunderlich curve construction assumes that the curve is a compressing mapping from a low-dimensional space into a 2D domain, the area of which is the same at each iteration level [22]. For our unit cells, we assume a constant thickness of the solid walls that incurs variations in the channel length relative to that of the Wunderlich curve. Hence, in the "fixed channel" case, when the area of a bounding square increases at each iteration step (in contrast to original construction approach of the Wunderlich curve), the channel length is elongated by a factor of 3^N relative to a. In the "fixed unit cell" case, the channel length increases as $3^N a - 1$.

4.1 "Fixed-channel" case

Figure 4 shows calculated dispersion relations for homogeneous waves propagating in UC1, UC2, and UC3 along ΓX direction in the reciprocal k-space. The horizontal axis indicates normalized wavenumber $k^* = a_{uc}k$, and the vertical axes depict frequencies f in kHz and normalized frequencies $f^* = fa_{uc}/c_0$. Note different frequency ranges for each unit cell. The analyzed frequencies are limited to a sub-wavelength range, i.e. up to about $fa_{uc}/c_0 = 0.5$. For UC1, we consider modes forming the lowest band gap and extending up to 9 kHz; for the UC2 and

UC3, the frequency range is restricted to first 4 band gaps, and thus, it is limited to 4 kHz and 500 Hz, respectively.

The dash-dot lines represent phase velocities of sound waves in lossless air for the lowets fundamental mode within a unit cell and in homogeneous air (when a unit cell is removed). As can be expected, the velocity slows down when a wave propagates through a labyrinthine channel. The velocity decreases by factors 1.63, 2.91, and 5.28, as compared to homogeneous air.

The dispersion relations in Fig. 2 are characterized by several frequency band gaps in the sub-wavelength region. All of them are located below $fa/c_0 = 0.45$. Hence, we conclude that the designed labyrinthine metamaterials can control sound waves at subwavelength scales. As *N* increases, the band gaps are shifted to lower frequencies. These shifts are directly related to the path elongation. For example, the 1st band gap starting from $fa/c_0 = 0.21$ for UC1, is shifted to about 3 times lower frequency, $fa/c_0 = 0.069$, for UC2, since the channel length in UC2 is 3 times longer than that in UC1.

The band gaps bounds are formed by flat parts of dispersion bands that describe localized modes. The corresponding pressure distribution are given in the 1st and 3rd columns of Table 1 for the 1st band gaps and Table 2 for the 2nd and 3rd band gaps. As green color indicates (almost) zero pressure, one can observe strong pressure localization within the labyrinthine channel. It is easy to find out that regardless of the iteration level, these localized modes correspond to Fabry-Perot resonances in a straight slit of width w and length L_{eff} [21, 13]:

$$f_l^{FP} = lc_0/2L_{eff}, \qquad (5)$$

whwre l is a positive integer. In the "fixed channel" case, L_{eff} equals $2.305d_{uc}$ for UC1; $L_{eff} = 5.667d_{uc}$ for UC2, and $L_{eff} = 16.642d_{uc}$ for UC3, where $d_{uc} = a_{uc}\sqrt{2}$. Note that odd values of l correspond to the lower band gap bounds,

while even values of l allow evaluating the upper band gap bounds in Fig. 2.

The fact that multiple harmonics of the Fabry-Perot resonances form the band gap bounds, explains a similar structure of the dispersion relation at various frequencies with close values of phase and group velocities for dispersion bands.

The pressure distributions in Tables 1 and 2 are also similar to those of the artificial monopole, dipole and multipole resonances [12]. For example, the patterns at lower bound of the 1st band gap (the 1st column in Table 1) resemble that of a monopole, when the pressure is concentrated in the central part of a channel and equally radiates along two propagation directions [12, 14]. Since an effective dynamic bulk modulus (not evaluated for our unit cells) is typically negative in a limited frequency range above the monopole resonance, one can expect a high wave reflectance at these frequencies [12]. The wave reflection and transmission characteristics for the labyrinthine structures are analyzed later in this section.

Apart from the Fabry-Perot resonances, wave dispersion in our labyrinthine metamaterials is also characterized by the presence of bands at the band gap frequencies. These bands can be found within each band gap for every analyzed unit cell (see Fig. 4). The pressure distributions at these modes (the 2nd column in Tables 1 and 2) resemble those for the dipole resonance and its higher harmonics (compare to 3rd column of Tables 1 and 2), but the pressure is not localized inside a channel. Thus, these modes do not represent standing waves of localized pressure, but are propagating ones with very slow (and often negative) group velocities. They are analogous to slow modes inside phononic band gaps for elastic waves [30, 31]. The mechanism of the slow mode excitation and its dynamics will be investigated in more detail in our future work. Here, we leave these modes within the band gaps

(instead of separating a band gap into two parts), since we have not detected the presence of these modes in the frequency-domain simulations, even for a very fine frequency step (see Figs. 5 and 7).

Frequency-domain simulation results are given in Figures 5 and 6 in terms of transmission and absorption coefficients for lossless and lossy air. We analyze wave propagation through a monolayer composed of the labyrinthine unit cells (Figs. 5a, 6a, 6c) and straight slits of length L_{eff} (Fig. 5b, 6b, 6d) and a_{uc} (Fig. 5c). (Note that at certain very low frequencies in lossy air, the transmission and absorption coefficients appeared to be mesh-dependent, and hence, are not shown as unreliable.)

When losses in air are neglected, for all the structures, incoming waves are either transmitted or reflected, and thus, the absorption coefficient is zero (not shown in the graphs). Total transmission is achieved at frequencies of the Fabry-Perot resonances (5). As can be seen, this effect is independent of the channel tortuosity and occurs in folded labyrinthine channels of any iteration level at almost the same frequencies as for straight slits. For the slit of length a_{uc}, the first Fabry-Perot resonance appears to be higher than the analyzed frequency range. This structure acts as a rigid scatterer at sub-wavelength frequencies, and thus, it will be not considered further. When thermos-viscous losses are included, the transmission peaks decrease in magnitude and are shifted to lower frequencies compared to the lossless case. The later occurs due to slowing down of the wave velocity in dissipative air, as confirmed by experimental measurements in [21].

The striking differences in wave dynamics of straight and fractal-shaped channels occur between the frequencies of Fabry-Perot resonances. In case of straight slits, the main part of incoming waves is reflected, while about 15-20%

of the wave energy is transmitted through a slit. For the labyrinthine metamaterials, the same behavior is observed in the propagating frequency range, while within the band gaps total wave reflection occurs with zero transmission coefficient. If we remember, that the lower band gap bounds are formed by the monopole resonance and its higher harmonics, then total reflectance is justified by a negative values of effective dynamic bulk modulus at the band gap frequencies. Note that 100% wave reflection is preserved even if thermos-viscous losses are taken into account. In contrast to the total transmission effect at Fabry-Perot resonances, which is eliminated by the loss mechanism, the total reflection is not affected by dissipation. As the iteration level increases, the band gaps, i.e. the total reflection frequencies, are shifted to lower frequencies and decrease in size (compare Figs. 5a, 6a, and 6c). However, the amount of transmitted energy at frequencies of propagating modes also decreases, that is not the case for the straight slits (compare e.g. Figs. 6c and 6d).

To summarize the results, we can derive two key conclusions. First, the wave characteristics of labyrinthine meta-materials with fractal-structured channels differ from those for straight slits of the effective length due to the tortuosity effect, which becomes important, when a wave is allowed to propagate in the opposite (to the main wave field) direction. Therefore, the derivation of effective characteristics for this type of metastructures should take into account the tortuosity effects. Second, the designed labyrinthine metamaterials can be used as broadband low-frequency sound reflectors of compact size, since 100% wave reflection can be achieved by using a single unit cell.

The circular markers in Fig. 5a represent the transmission values for the corresponding 3D domain, which is obtained by extruding the 2D model in

Fig.2 in the out-of-plane direction by height $4a_{uc}$. An excellent agreement between the 3D and 2D results justifies the introduced assumption on the two-dimensional character of the analyzed problem.

Finally, we note that the designed labyrinthine metamaterials can be considered as tortuous open-porous materials. The porosity level, evaluated as ratio of the area of air inside a unit cell to the total area of a unit cell, is 0.901 for UC1, 88 % for UC2, and 89 % for UC3, which is rather low compared to porosity of typical foams that is very close to 1 [32]. However, the main difference between the porous materials and the designed labyrinthine metastructures is the physical mechanism of the wave control. Porous materials attenuate waves due to thermos-viscous losses with the absorption coefficient close to 1 for broadband frequencies. In contrast, the designed structures mainly reflect incident waves with absorption hardly approaching 0.5 for single frequencies (see Figs. 6 a,c). In the next section, we evaluate the metamaterial performance for increased level of thermo-viscous losses.

4.2 "Fixed-unit-cell" case

Dispersion relations for UC1 and UC2 for the "fixed unit cell" case, when $a_{uc} =$ 14 mm, are shown in Fig. 7 for homogeneous waves along ΓX direction. The dimensional frequency ranges are the same as those for the corresponding unit cells in the "fixed channel" case (see Figs. 4 a,b).

The structure of the dispersion relation in Fig. 7a is similar to that in Fig. 4a, except that the dispersion bands are shifted to higher frequencies due to a shorter length of the labyrinthine channel. From the first sight, more differences can be found by comparing the dispersion relations for UC2 in Fig. 4b and Fig. 7b. While in Fig. 4b there are four band gaps, the relation in Fig. 7b is characterized by the presence

of a single wide band gap. This happens because the unit cell area, $A^{(fix_{uc})} = 14^2$ mm^2, in the second case is about 3 times smaller than that for the "fixed channel case", $A^{(fix_w)} = 41^2$mm^2. This causes shift of the monopole, dipole and multipole resonances, and thus, the related band gaps, to 3 times higher frequencies. However, for the non-dimensional frequencies, the band gaps remain unchanged. In general, it can be expected, that the dispersion relations for the two considered cases must be the same for non-dimensional frequencies, since the metamaterial structure is preserved. In contrast to this, we should observe differences in the transmission and absorption coefficients for lossy air in the two cases due to various amount of thermo-viscous losses in the channels of a different width.

Figure 8 shown the transmission and absorption coefficients for the labyrithine monoslabs of "fixed unit cell" case and those for straight slits of the corresponding length. In general, the features found by analyzing the "fixed channel" case are also observed in the present case. Namely, the wave propagation in the labyrinthine channels is not equivalent to that in the straight slits due to the presence of 100% reflection within band gap frequencies, which is independent of dissipation in air. However, as the channel in the "fixed unit cell" case is more than 4 times narrower relative to that in the "fixed channel" case, the influence of thermos-viscous losses is more pronounced that can be seen in larger absorption values at the Fabry-Perot resonant frequencies.

Therefore, wave attenuation within labyrinthine channels can be obviously increased by decreasing the channel width. In contrast to this, the porosity of the metamaterial decreases. Thus, for UC2, the structural porosity is 0.647 for the "fixed unit cell" case versus 0.88 for the "fixed channel" case. Thus, one can approach the functionality of the

designed labyrinthine metamaterials to that of tortuous porous materials by decreasing the structural external dimensions and porosity.

5. Conclusions

In this work, we theoretically analyzed the possibilities of labyrinthine acoustic metamaterials with sub-wavelength channels shaped along a space-filling curve to control airborne homogeneous sound waves. We demonstrated that, if an internal channel allows wave propagation in the opposite (to the incident pressure field) direction, the dynamics of the folded channel is not equivalent to that of a straight slit of an effective length. In particular, we found out that Fabry-Perot resonances of a straight slit correspond to the monopole, dipole and multipole resonances in folded channels and govern the generation of band gaps. Within the band gaps, total wave reflection occurs that is not influenced by the presence of dissipation in air. Moreover, by increasing the channel tortuosity and further elongating a wave path, one can achiev 100% reflection outside band gaps. Despite the fact that for higher iteration levels, the designed labyrinthine metamaterials resemble tortuous porous structure, they control wave propagation due to wave interference effects, in contrast to thermos-viscous dissipation in porous structures. This results in a low wave attenuation within a metastructure. We show that the absorption can be increased by decreasing the channel width and the structural dimensions.

This is the first time that a fractal space-filling curve has been considered for designing wave paths in labyrinthine metamaterials, and thus, further more in-depth analysis is required to analyze the influence of various factors, e.g. number of turns or an angle of turn, as well as the performance for inhomogeneous waves, on wave dynamics in channels of such a complex form. This studies will be performed in our future work. In conclusion, we believe that the proposed

structures could be of use as a new type of broadband low-frequency sound reflectors that can be inexpensively assembled from thin equal sheets by arranging them along indicated paths.

Acknowledgement

A.O.K. acknowledges Dr. Dmitry Krushinsky (University of Wageningen, the Netherlands) for the continuous support of this work and fruitful discussions. A.O.K. is supported by the funding from the European Union's 7th Framework programme for research and innovation under the Marie Skłodowska-Curie Grant Agreement No. 609402-2020 researchers: Train to Move (T2M). N.M.P. is supported by the European Research Council (ERC PoC 2015 SILKENE No. 693670), and by the European Commission under the Graphene FET Flagship (WP14 "Polymer Nanocomposites" No. 604391) and FET Proactive "Neurofibres" grant No. 732344. FB is supported by "Neurofibres" grant No. 732344.

References

[1] S. Cummer, J. Christensen and A. Alu, "Controlling sound with acoustic metamaterials," *Nat. Rev. Mats.,* vol. 16001, 2016.

[2] R. V. Craster and S. Guenneau, Acoustic Metamaterials: Negative Refraction, Imaging, Lensing and Cloaking, Heidelberg: Springer, 2012.

[3] Z. Liu, X. Zhang, Y. Mao, Y. Y. Zhu, Z. Yang, C. Chan and P. Sheng, "Locally resonant sonic materials," *Science,* vol. 289, p. 1734, 2000.

[4] A. Krushynska, V. Kouznetsova and M. Geers, "Towards optimal design of locally resonant acoustic metamaterials," *J. Mech. Phys. Solids,* vol. 71, p. 179–196, 2014.

[5] P. Deymier, Acoustic metamaterials and phononic structures, Heidelberg: Springer, 2013.

[6] N. Fang, D. Xi, J. Xu, M. Ambati, W. Srituravanich, C. Sun and X. Zhang, "Ultrasonic metamaterials with negative modulus," *Nat. Mat.,* vol. 5, pp. 452-456, 2006.

[7] A. Movchan and S. Guenneau, "Split-ring resonators and localized modes," *Phys. Rev. B,* vol. 70, p. 125116, 2004.

[8] G. Ma, M. Yang, S. Xiao, Z. Yang and P. Sheng, "Acoustic metasurface with hybrid resonances," *Nat. Mat.,* vol. 13, pp. 873-878, 2014.

[9] Z. Yang, J. Mei, M. Yang, N. H. Chan and P. Sheng, "Membrane-type acoustic metamaterial with negative dynamic mass," *Phys. Rev. Lett.,* vol. 101, p. 204301, 2008.

[10] V. García-Chocano and J. Sánchez-Dehesa, "Anomalous sound absorption in lattices of cylindrical perforated shells," *Appl. Phys. Lett.,* vol. 106, no. 12, p. 124104, 2015.

[11] A. Bozhko, J. Sanchez-Dehesa and A. Krokhin, "Redirection and splitting of sound waves by a periodic chain of thin perforated cylindrical shells," *J. Acoust. Soc. Am.,* vol. 141, p. 3640, 2017.

[12] Y. Cheng, C. Zhou, B. Yuan, D. Wu, Q. Wei and X. Liu, "Ultra-sparse metasurface for high reflection of low-frequency sound based on artificial Mie resonances," *Nat. Mater.,* vol. 14, pp. 1013-1019, 2015.

[13] Z. Liang and J. Li, "Extreme acoustic metamaterial by coiling up space," *Phys. Rev. Lett.,* vol. 108, p. 114301, 2012.

[14] A. Krushynska, F. Bosia, M. Miniaci and N. Pugno, "Tunable spider-web inspired hybrid labyrinthine acoustic metamaterials for low-frequency sound control," *arXiv:1701.07622,* 2017.

[15] Z. Liang, T. Feng, S. Lok, F. Liu, K. Ng, C. Chan, J. Wang, S. Han, S. Lee and J. Li, "Space-coiling metamaterials with double negativity and conical dispersion," *Sci. Rep.,* vol. 3, p. 1614, 2013.

[16] Y. Xie, B.-I. Popa, L. Zigoneanu and S. Cummer, "Measurement of a broadband negative index with space-coiling acoustic metamaterials," *Phys. Rev. Lett.,* vol. 110, p. 175501, 2013.

[17] T. Frenzel, J. Brehm, T. Bueckmmann, R. Schitty, M. Kadic and M. . Wegener, "Three-dimensional labyrinthine acoustic metamaterials," *Appl. Phys. Lett.,* vol. 103, p. 061907, 2013.

[18] C. Zhang and X. Hu, "Three-dimensional single-port labyrinthine acoustic metamaterial: perfect absorption with large bandwidth and tunability," *Phys. Rev. Appl.,* vol. 6, p. 064025, 2016.

[19] Y. Xie, A. Konneker, B.-I. Popa and S. Cummer, "Tapered labyrinthine acoustic metamaterials for broadband impedance matching," *Apl. Phys. Lett.,* vol. 103, p. 201906, 2013.

[20] G. Song, Q. Cheng, B. Huang, H. Y. Dong and T. Cui, "Broadband fractal acoustic metamaterials for low-frequency sound attenuation," *Appl. Phys. Lett.,* vol. 109, p. 131901, 2016.

[21] M. Moleron, M. Serra-Garcia and C. Daraio, "Visco-thermal effects in acoustic metamaterials: from total transmission to total reflection and high absorption," *New J. Phys.,* vol. 18, p. 033003, 2016.

[22] H. Sagan, Space-filling curves, Springer, 1994.

[23] G. Peano, "Sur une courbe, qui remplit toute une aire plane," *Math. Ann.,* vol. 36, no. 1, pp. 157-160, 1890.

[24] H. Haverkort and F. van Walderveen, "Locality and bounding-box quality of two-dimensional," *Computational Geometry: Theory and Applications,* vol. 43, pp. 131-147, 2010.

[25] J. K. Lawder and P. J. H. King, "Using Space-Filling Curves for Multi-dimensional Indexing," *Advances in Databases. BNCOD 2000. Lecture Notes in Computer Science,* vol. 1832, 2000.

[26] M. Ali and S. Ladhake, "Overview of space-filling curves and their applications in scheduling," *International Journal of Advances in Engineering and Technology,* vol. 1, no. 4, pp. 148-154, 2011.

[27] L. Platzman and J. I. Bartholdi, "Spacefilling curves and the planar travelling salesman problem," *Journal of the ACM,* vol. 36, no. 4, pp. 719-737, 1989.

[28] Acoustics Module. User's guide, 2013.

[29] w. R. 5. Comsol Multiphysics.

[30] R. Zhu, X. Liu, G. Hu, F. Yuan and G. Huang, "Microstructural designs of plate-type elastic metamaterial and their potential applications: a review," *Int. J. Smart and Nano Mater.,* vol. 6, no. 1, pp. 14-40, 2015.

[31] C.-Y. Sun, J.-C. Hsu and T. Wu, "Resonant slow modes in phononic crystal plates with periodic membranes," *Appl. Phys. Lett.,* vol. 97, p. 031902, 2010.

[32] J. Allard and N. Atalla, Propagation of sound in porous media: modelling sound absorbing materials, Willey, 2009.

List of figures

Figure 1. (a) Unit cell of the 1st iteration level (UC1) with dimensions. Labyrinths with air channels shaped according to the Wunderlich space-filling curve of the first three iteration levels incorporated into UC1, UC2, and UC3. Solid walls of constant thickness, d = 0.5mm, are indicated in blue. The wave propagation direction is shown by blue arrows in (b).

Figure 2. Schematic of the frequency domain model. Green area corresponds to an air domain, green dashed lines indicate locations, at which reflection and transmission coefficients are evaluated. The plane wave radiation condition is applied along the bold red line.

Figure 3. Thickness of viscous δ_{vis} and thermal δ_{th} boundary layers according to relations (3) and (4).

Figure 4. **"Fixed channel" case**: Dispersion relations for the labyrinthine unit cells of the 3 iteration levels with a fixed channel width, w=4 mm. Band gaps are shown by shaded rectangles. The slope of the green and red dash-dot lines indicates phase velocities of the fundamental mode

within a unit cell and in homogenous air (when a unit cell is removed). Bold points designate frequencies with the pressure distributions given in Table 1 and 2.

Figure 5. **"Fixed channel" case:** Transmission (T) and absorption (A) coefficients for acoustic waves in lossless (dashed line) and lossy (solid line) air through (a) a labyrinthine metamaterial UC1; (b) a straight slit of width $w = 4$ mm and length L_{eff} = 45.6 mm; (b) a straight slit of width $w = 4$ mm and length a_{uc} = 18 mm. Shaded regions indicate frequency a band gap shown in Fig. 4a. Circular markers in (a) indicate transmission coefficient values in lossless air for the corresponding 3D model of height $4a_{uc}$.

Figure 6. **"Fixed channel" case:** Transmission (T) and absorption (A) coefficients for acoustic waves in lossless (dotted line) and lossy (solid line) air through (a) a labyrinthine metamaterial UC2 and (b) a straight slit of width $w = 4$ mm and length L_{eff} = 328.5 mm; (c) a labyrinthine unit cell UC3 and (d) a straight slit of width $w = 4$ mm and length L_{eff} = 2.871 m. Shaded regions indicate frequency band gaps shown in Fig. 4.

Figure 7. **"Fixed unit cell" case**: Band structure diagrams for the unit cells UC1 and UC2 of fixed size a=14 mm with the channel width of 3 mm and 0.9 mm, respectively. Band gap frequencies are shaded. The slopes of the green and red dash-dot lines indicate the phase velocities of the fundamental pressure wave inside a unit cell and in homogeneous air (when a unit cell is removed).

Figure 8. **"Fixed unit cell" case:** Transmission (T) and absorption (A) coefficients for acoustic waves in lossless (dotted line) and lossy (solid line) air through (a) a labyrinthine unit cell UC1 and (b) a straight slit of width $w = 3$ mm and length L_{eff} = 34.6 mm; (c) a labyrinthine unit cell UC2 and (d) a straight slit of width $w = 0.9$ mm and length L_{eff} = 107 mm. Shaded regions indicate frequency band gaps shown in Fig. 7.

List of tables

Table 1. **"Fixed channel" case ("Fixed unit cell" case):** Pressure distributions around the 1st band gap for the labyrinthine metamaterial unit cells of the 3 iteration levels. Red and blue colors represent maximum and minimum pressure, while green color indicates (almost) zero pressure. The frequencies in brackets are referred to the "fixed unit cell" case.

Table 2. **"Fixed channel" case**: Pressure distributions around the 2nd and 3rd band gaps for the labyrinthine metamaterial unit cells of the 2nd and 3rd iteration levels. Red and blue colors represent maximum and minimum pressure, and green color indicates (almost) zero pressure.

Figures

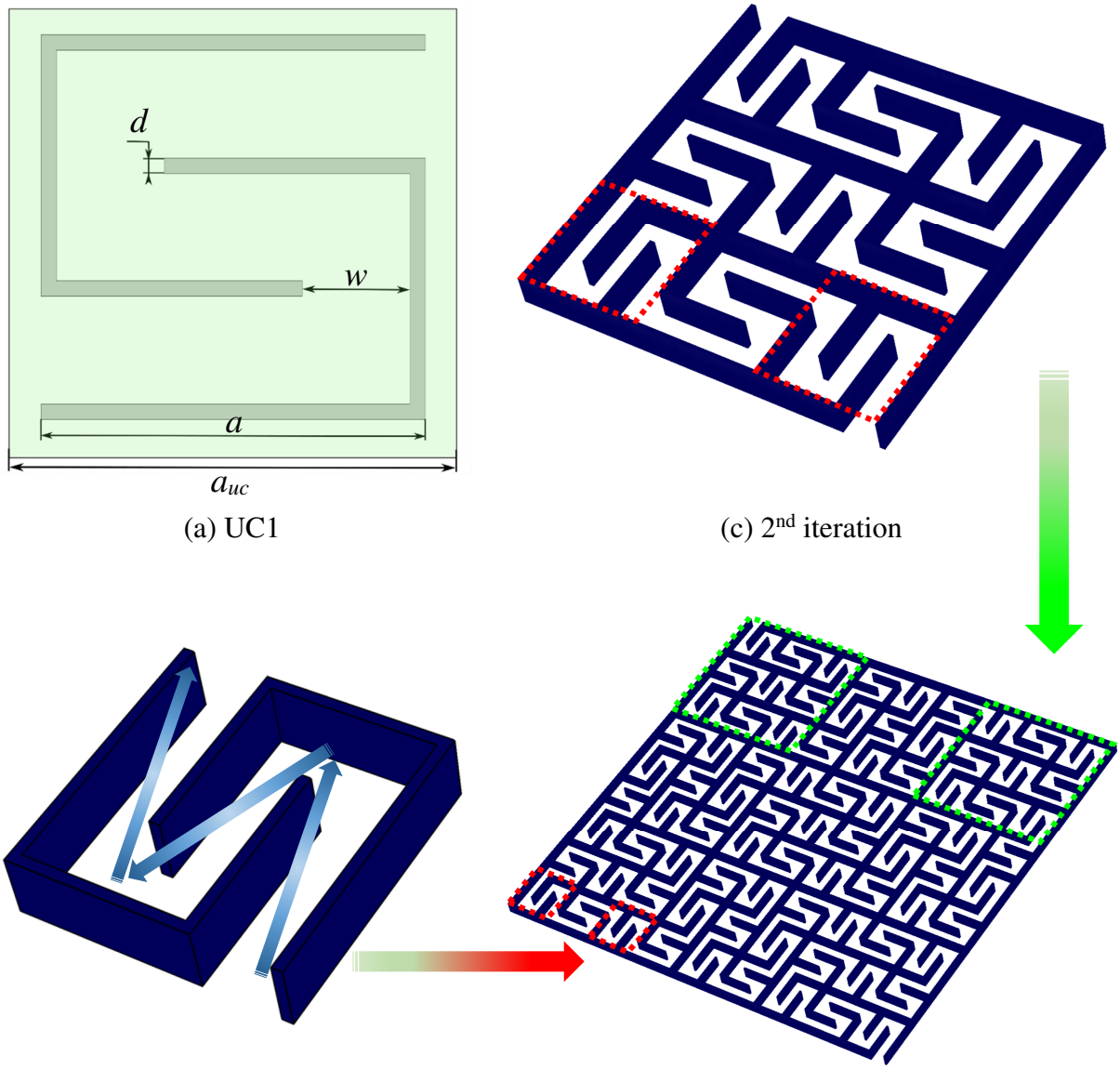

(a) UC1

(c) 2nd iteration

(b) 1st iteration

(d) 3rd iteration

Figure 1. (a) Unit cell of the 1st iteration level (UC1) with dimensions. (b-d) Labyrinths with air channels shaped according to the Wunderlich space-filling curve of the first three iteration levels incorporated into UC1, UC2, and UC3. Solid walls are indicated in blue. The shortest path taken by a wave within UC1 is shown by blue arrows in (b).

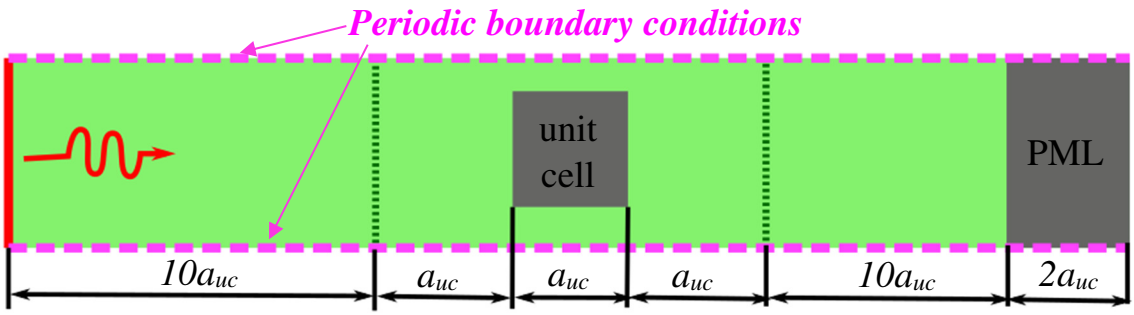

Figure 2. Schematic of the frequency domain model. Green area corresponds to an air domain, green dashed lines indicate locations, at which reflection and transmission coefficients are evaluated. The plane wave radiation condition is applied along the bold red line.

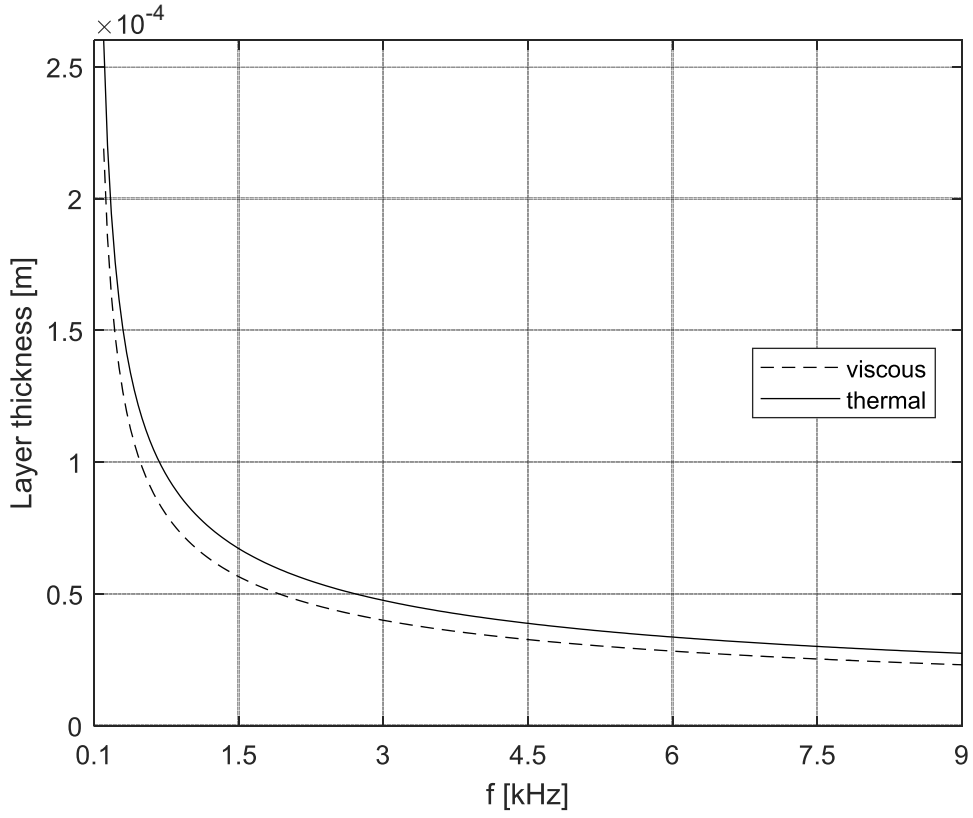

Figure 3. Thickness of viscous δ_{vis} and thermal δ_{th} boundary layers according to relations (3) and (4).

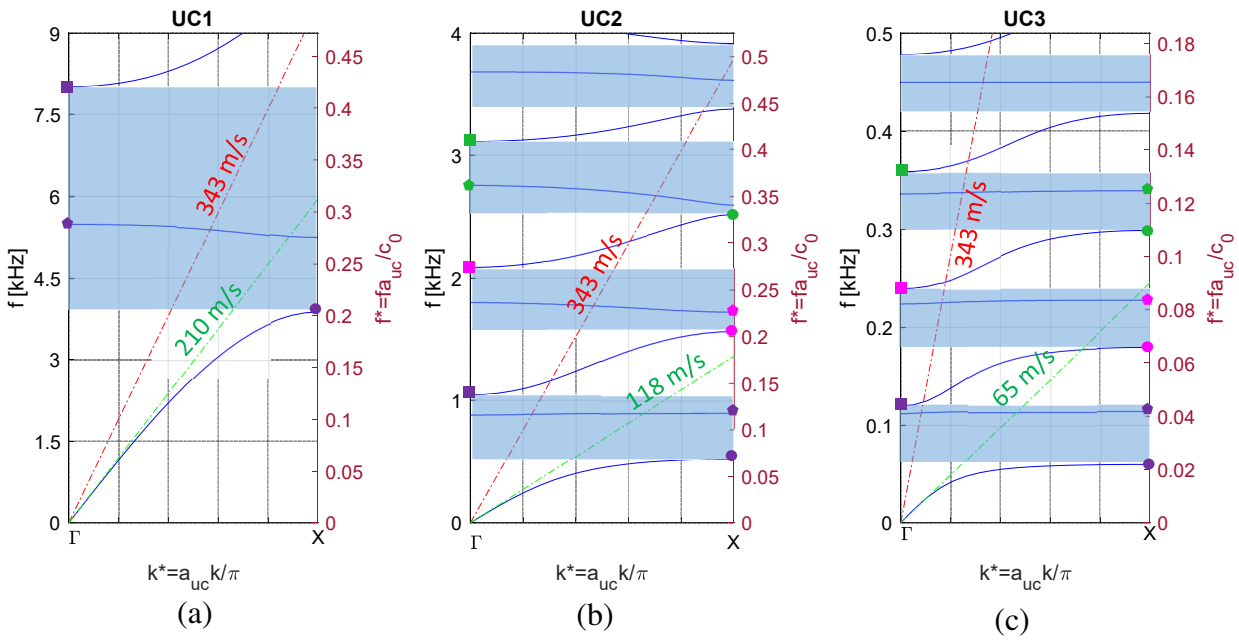

Figure 4. ***"Fixed channel" case****: Dispersion relations for the labyrinthine unit cells of the 3 iteration levels with a fixed channel width, w=4 mm. Band gaps are shown by shaded rectangles. The slope of the green and red dash-dot lines indicates phase velocities of the fundamental mode within a unit cell and in homogenous air (when a unit cell is removed). Bold points designate frequencies with the pressure distributions given in Table 1 and 2.*

Table 1. ***"Fixed channel" case ("Fixed unit cell" case):*** *Pressure distributions around the 1st band gap for the labyrinthine metamaterial unit cells of the 3 iteration levels. Red and blue colors represent maximum and minimum pressure, while green color indicates (almost) zero pressure. The frequencies in brackets are referred to the "fixed unit cell" case.*

	● **Lower bound**	■ **Internal mode**	⬟ **Upper bound**
UC1, 1st band gap	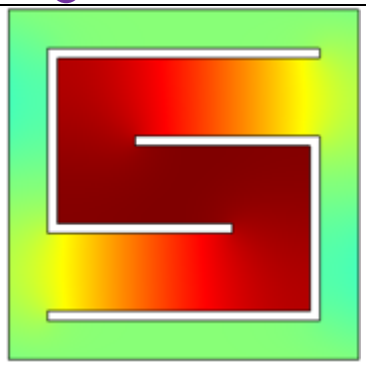 (a) 3876 Hz (4960 Hz)	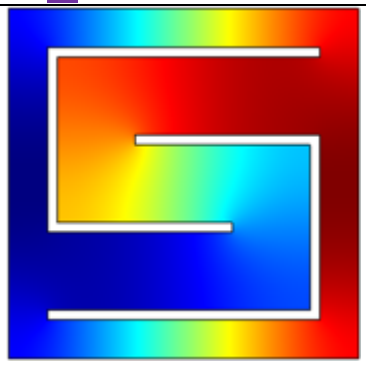 (b) 5250 Hz (7007 Hz)	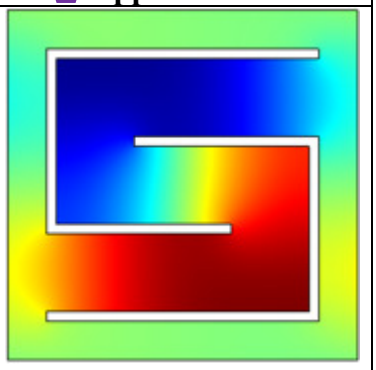 (c) 8011 Hz
UC2, 1st band gap	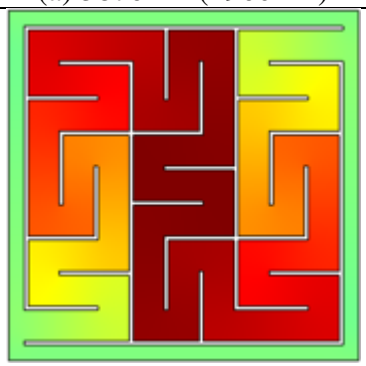 (d) 522 Hz (1602 Hz)	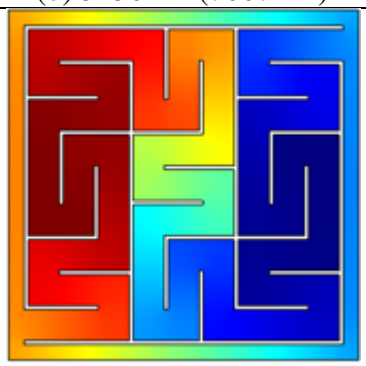 (e) 900 Hz (2782 Hz)	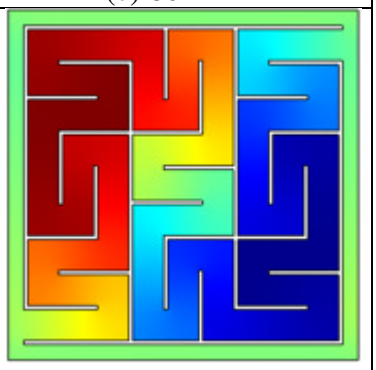 (f) 1045 Hz (3207 Hz)
UC3, 1st band gap	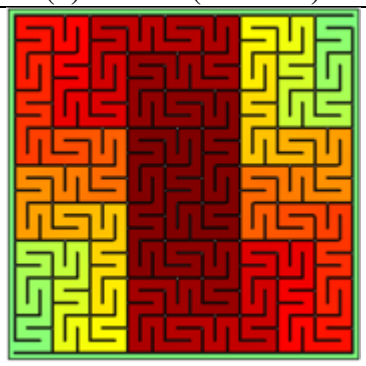 (g) 60 Hz	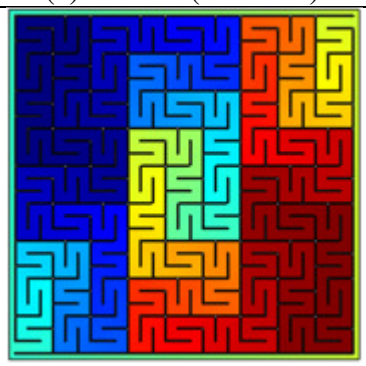 (h) 114 Hz	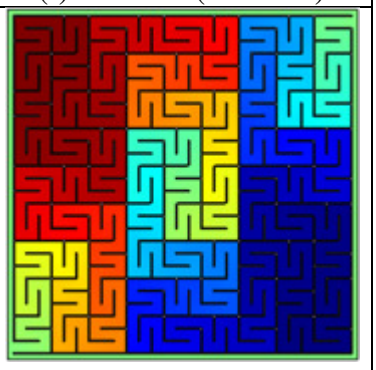 (i) 120 Hz

Table 2. ***"Fixed channel" case****: Pressure distributions around the 2nd and 3rd band gaps for the labyrinthine metamaterial unit cells of the 2nd and 3rd iteration levels. Red and blue colors represent maximum and minimum pressure, and green color indicates (almost) zero pressure.*

	● **Lower bound**	■ **Internal mode**	⬟ **Upper bound**
UC2, 2nd band gap	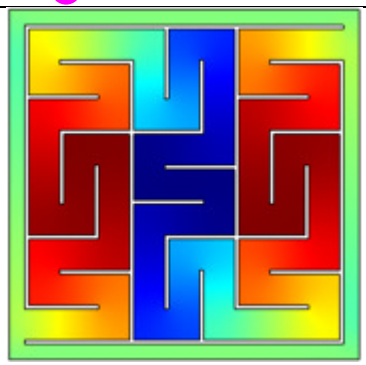 (a) 1566 Hz	 (b) 1726 Hz	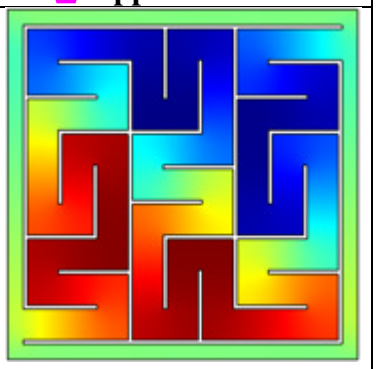 (c) 2086 Hz
UC3, 2nd band gap	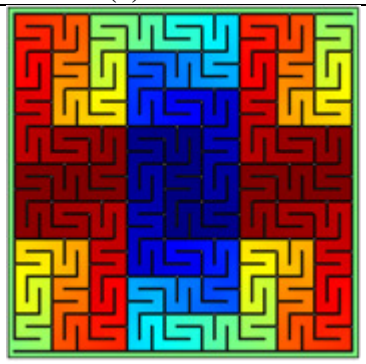 (d) 179 Hz	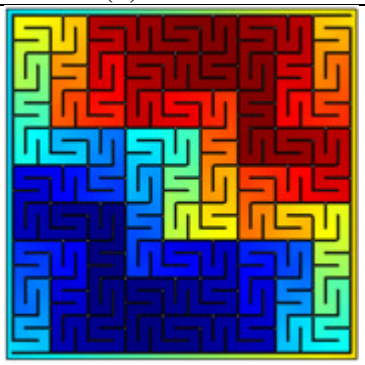 (e) 277 Hz	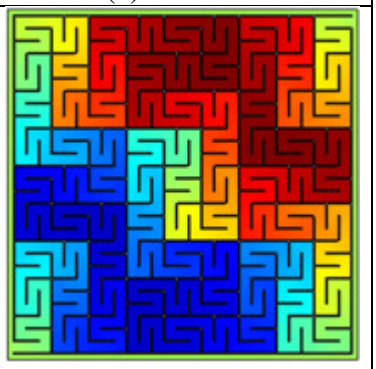 (f) 239 Hz
	● **Lower bound**	■ **Internal mode**	⬟ **Upper bound**
UC2, 3rd band gap	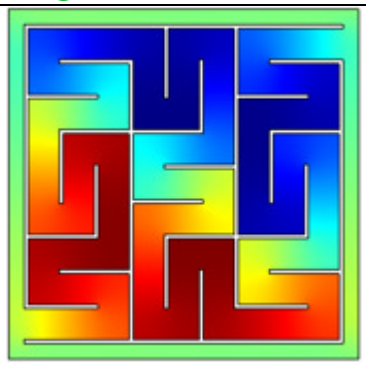 (g) 2520 Hz	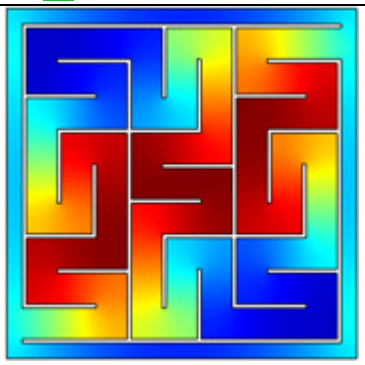 (h) 2757 Hz	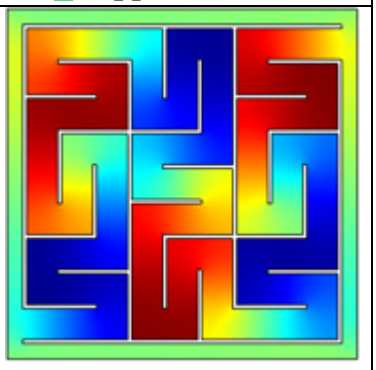 (i) 3114 Hz

UC3, 3rd band gap	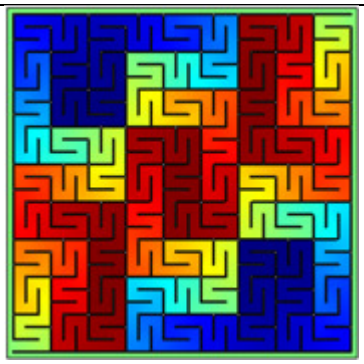	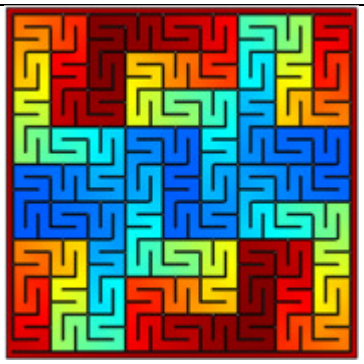	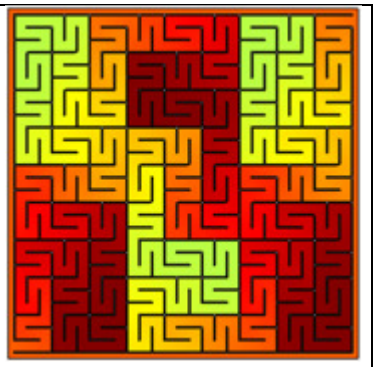
	(j) 299 Hz	(k) 337 Hz	(l) 358 Hz

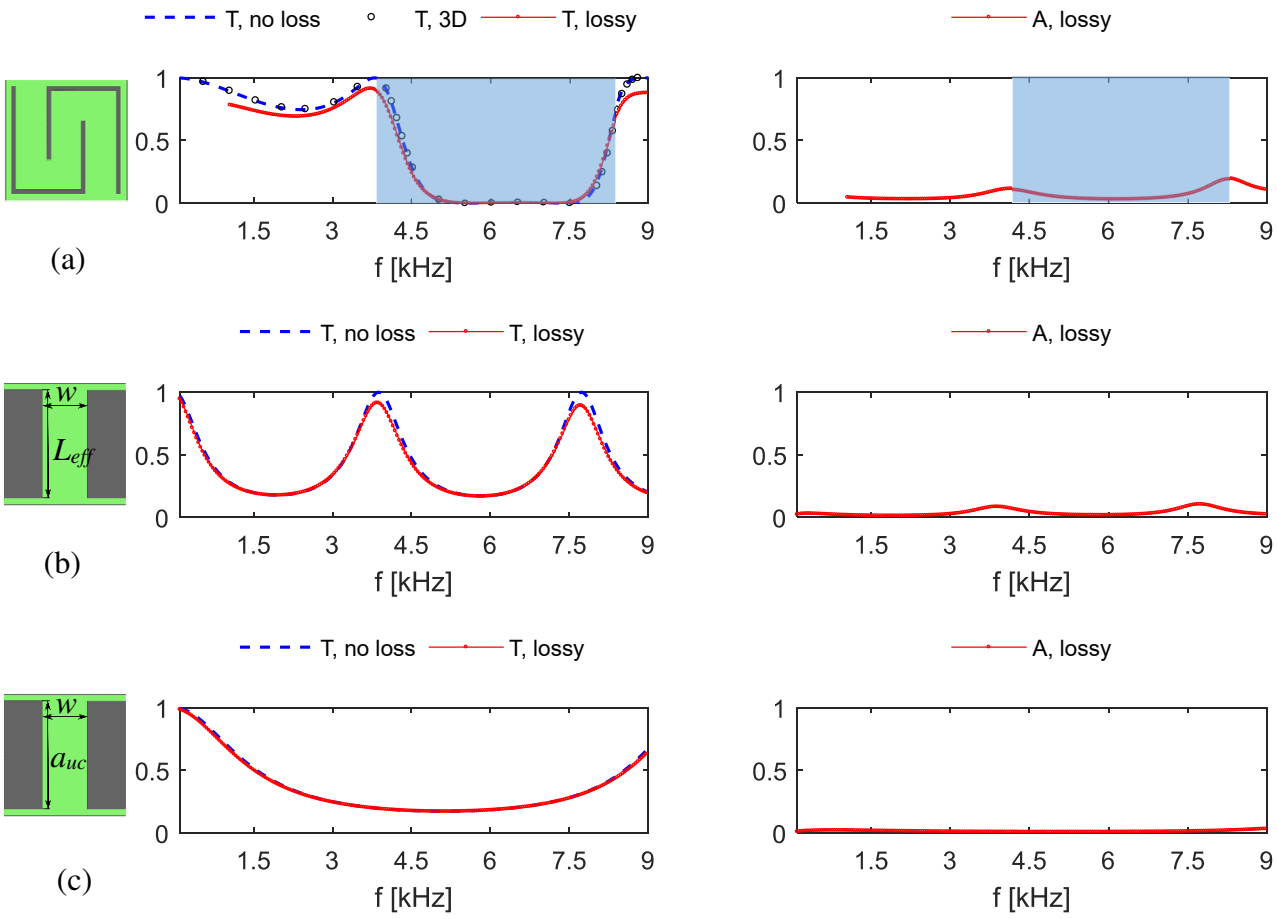

Figure 5. ***"Fixed channel" case:*** *Transmission (T) and absorption (A) coefficients for acoustic waves in lossless (dashed line) and lossy (solid line) air through (a) a labyrinthine metamaterial UC1; (b) a straight slit of width* $w = 4$ *mm and length* $L_{eff} = 45.6$ *mm; (b) a straight slit of width* $w = 4$ *mm and length* $a_{uc} = 18$ *mm. Shaded regions indicate frequency a band gap shown in Fig. 4a. Circular markers in (a) indicate transmission coefficient values in lossless air for the corresponding 3D model of height* $4a_{uc}$.

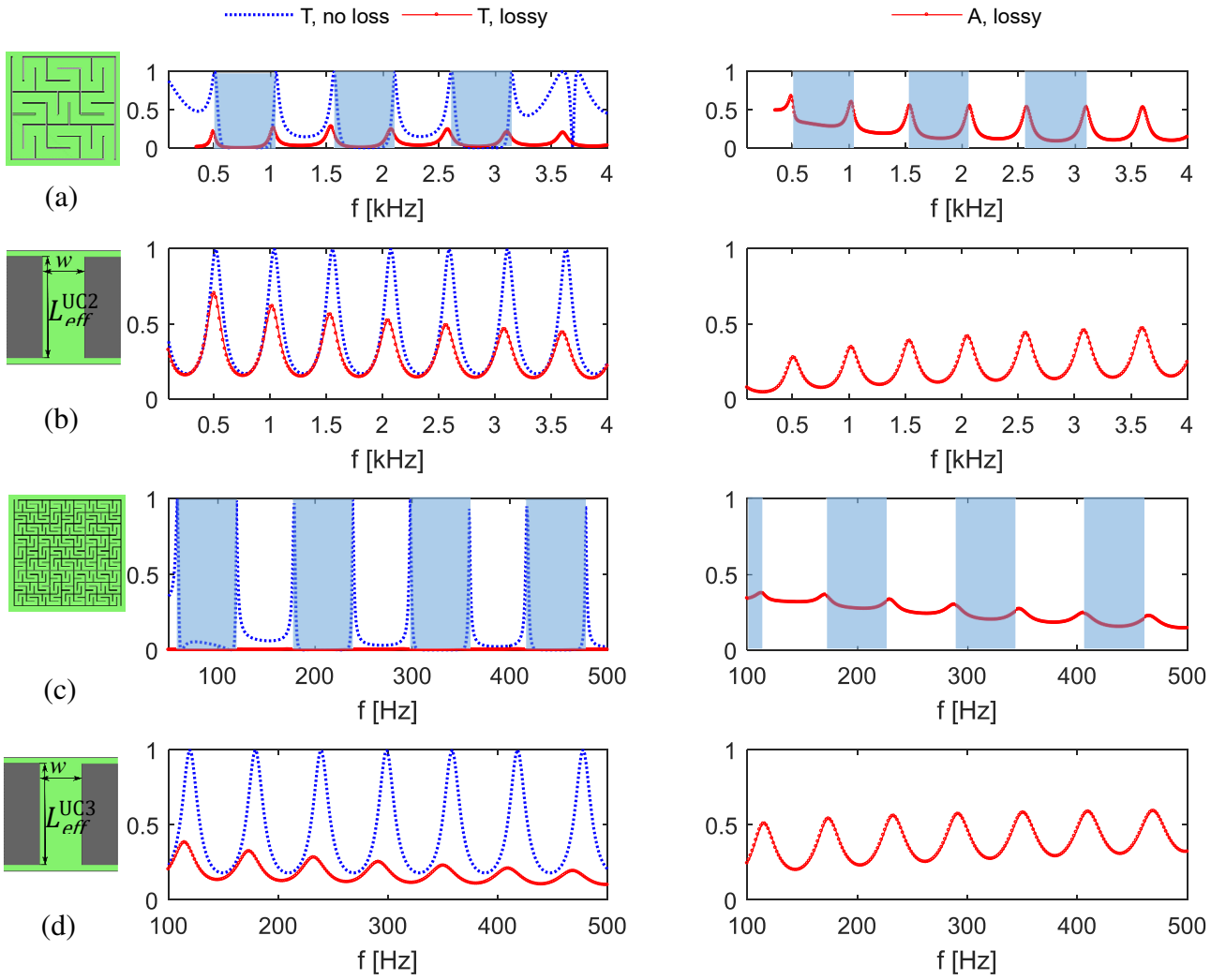

Figure 6. ***"Fixed channel" case:*** *Transmission (T) and absorption (A) coefficients for acoustic waves in lossless (dotted line) and lossy (solid line) air through (a) a labyrinthine metamaterial UC2 and (b) a straight slit of width* $w = 4$ *mm and length* L_{eff} *= 328.5 mm; (c) a labyrinthine unit cell UC3 and (d) a straight slit of width* $w = 4$ *mm and length* L_{eff} *= 2.871 m. Shaded regions indicate frequency band gaps shown in Fig. 4.*

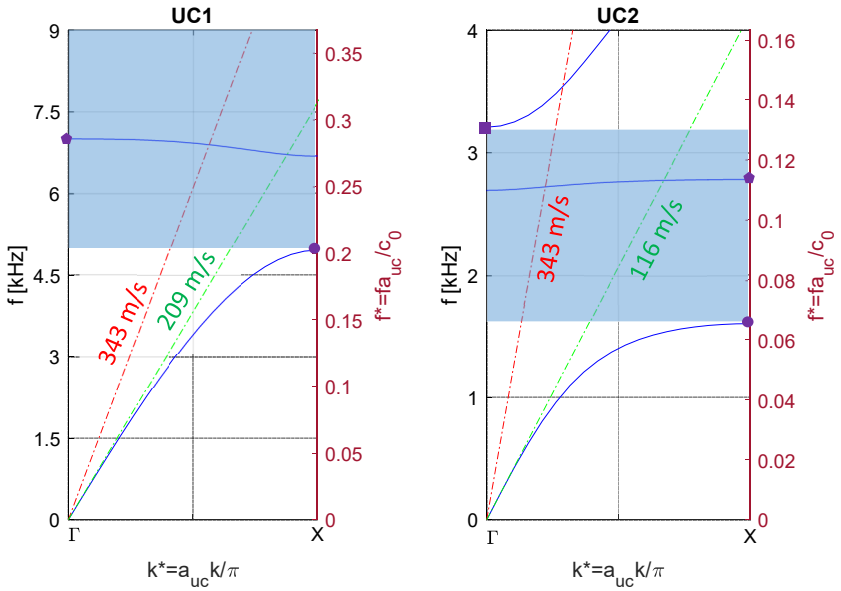

Figure 7. ***"Fixed unit cell" case****: Band structure diagrams for the unit cells UC1 and UC2 of fixed size a=14 mm with the channel width of 3 mm and 0.9 mm, respectively. Band gap frequencies are shaded. The slopes of the green and red dash-dot lines indicate the phase velocities of the fundamental pressure wave inside a unit cell and in homogeneous air (when a unit cell is removed).*

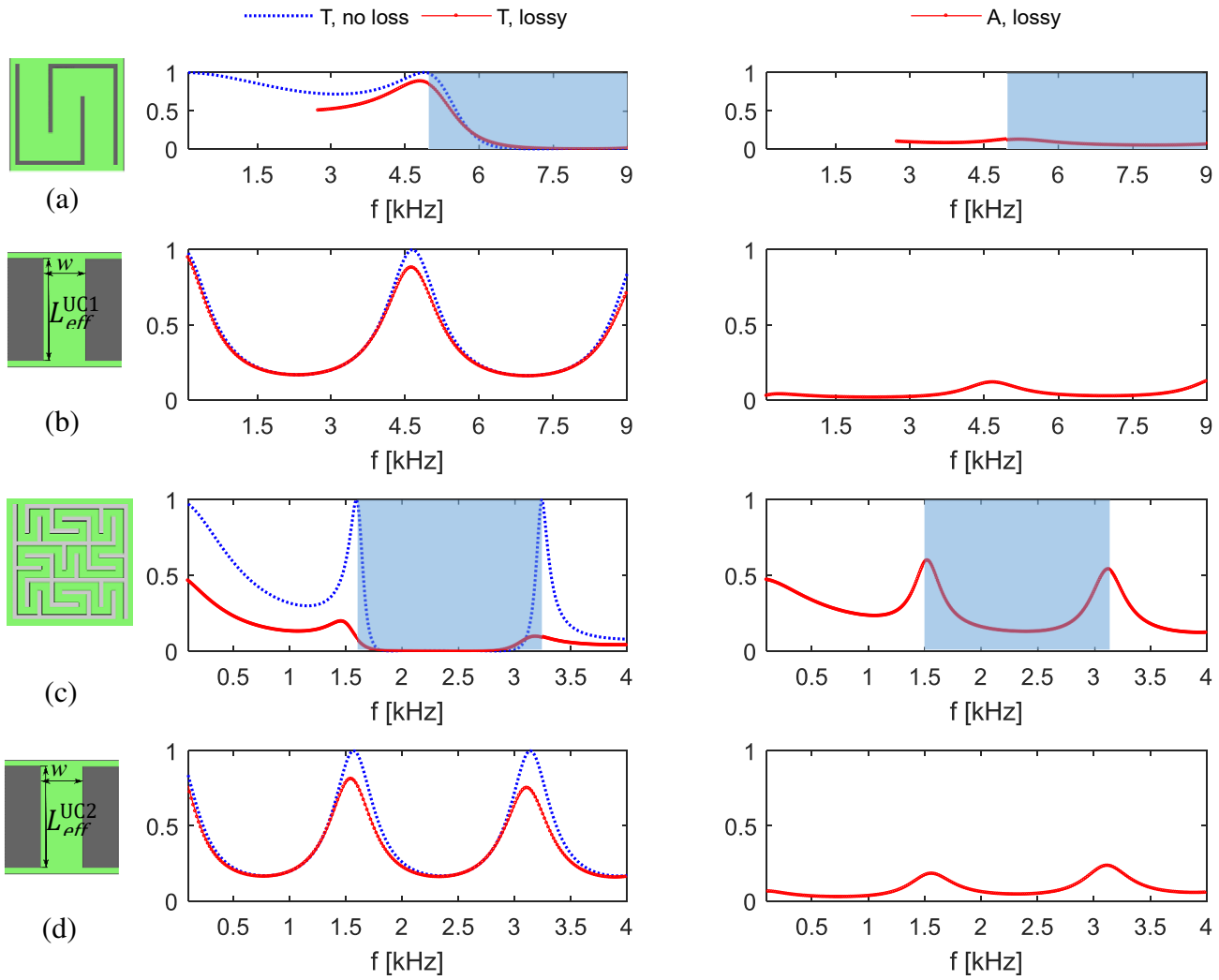

Figure 8. ***"Fixed unit cell" case:*** *Transmission (T) and absorption (A) coefficients for acoustic waves in lossless (dotted line) and lossy (solid line) air through (a) a labyrinthine unit cell UC1 and (b) a straight slit of width* $w = 3$ *mm and length* $L_{eff} = 34.6$ *mm; (c) a labyrinthine unit cell UC2 and (d) a straight slit of width* $w = 0.9$ *mm and length* $L_{eff} = 107$ *mm. Shaded regions indicate frequency band gaps shown in Fig. 7.*